

PCCP

Accepted Manuscript



This is an *Accepted Manuscript*, which has been through the Royal Society of Chemistry peer review process and has been accepted for publication.

Accepted Manuscripts are published online shortly after acceptance, before technical editing, formatting and proof reading. Using this free service, authors can make their results available to the community, in citable form, before we publish the edited article. We will replace this *Accepted Manuscript* with the edited and formatted *Advance Article* as soon as it is available.

You can find more information about *Accepted Manuscripts* in the [Information for Authors](#).

Please note that technical editing may introduce minor changes to the text and/or graphics, which may alter content. The journal's standard [Terms & Conditions](#) and the [Ethical guidelines](#) still apply. In no event shall the Royal Society of Chemistry be held responsible for any errors or omissions in this *Accepted Manuscript* or any consequences arising from the use of any information it contains.

ARTICLE

Seeded Growth of Ferrite Nanoparticles from Mn oxides : Observation of Anomalies in Magnetic Transitions

Cite this: DOI: 10.1039/x0xx00000x

Hyon-Min Song,^{*abc} Jeffrey I. Zink^b and Niveen M. Khashab^cReceived 00th January 2012,
Accepted 00th January 2012

DOI: 10.1039/x0xx00000x

www.rsc.org/

A series of magnetically active ferrite nanoparticles (NPs) are prepared by using Mn oxide NPs as seeds. Verwey transition is identified in Fe_3O_4 NPs with an average diameter of 14.5 nm at 96 K, where a sharp drop of magnetic susceptibility occurs. In MnFe_2O_4 NPs, spin glass-like state is observed with the decrease of magnetization below the blocking temperature due to the disordered spins during the freezing process. From these MnFe_2O_4 NPs, $\text{MnFe}_2\text{O}_4@\text{Mn}_x\text{Fe}_{1-x}\text{O}$ core-shell NPs are prepared by seeded growth. The structure of core is cubic spinels ($Fd-3m$), and shell is composed of iron-manganese oxide ($\text{Mn}_x\text{Fe}_{1-x}\text{O}$) with a rock salt structure ($Fm-3m$). Moiré fringes appear perpendicular to $\langle 110 \rangle$ directions on the cubic shape NPs through the plane-matched epitaxial growth. These fringes are due to the difference in their lattice spacings between MnFe_2O_4 and $\text{Mn}_x\text{Fe}_{1-x}\text{O}$. Exchange bias is observed in these $\text{MnFe}_2\text{O}_4@\text{Mn}_x\text{Fe}_{1-x}\text{O}$ core-shell NPs with an enhanced coercivity as well as the shift of hysteresis along the field direction.

Introduction

Soft ferrites are appealing materials for their spontaneous magnetization. Though as classical as other materials, they still extend their applications with nanosize ferrites, for example as more efficient contrast agents for magnetic imaging,¹ or as hyperthermia materials.² Equally interesting and important as this magnetic activity of soft ferrites will be their electrotechnical properties.^{3,4} Verwey transition is one of them and it is firstly known as a metal-insulator transition of magnetite (Fe_3O_4) at around 120 K, below which sudden decrease of conductivity occurs.^{5,6} A common finding is that when the size of magnetite is sufficiently small, the transition is not well observed or it is lower than 120 K.⁷⁻⁹ In general, metal-insulator transition in case of magnetite is believed due to the charge ordering below the transition temperature. In inverse spinel, octahedral sites are randomly occupied with even number of Fe^{2+} and Fe^{3+} , and tetrahedral sites with Fe^{3+} . Over the transition temperature, random arrangement of Fe^{2+} and Fe^{3+} in the octahedral sites makes the electron hopping possible, but below the transition temperature these ions are ordered without hopping.⁵ This charge ordering is accompanied by the unit cell change of ferrite from well-known cubic spinel to monoclinic. All these electronic features reflect the diversity and the dynamic nature of soft ferrites.

It is known that small amount of dopants affect Verwey transition temperature, mostly lowering below 120 K.

Impurities include metal ions such as Al,¹⁰ Mn,¹¹ and Zn.¹² Not only impurities, small cationic vacancy can also make the transition lower or disappear, such as $\text{Fe}_{3-\delta}\text{O}_4$ with $\delta = 0.066$.¹³ Also interesting is that Verwey transition is not limited to magnetite. Similar charge ordering and the phase transition were observed at around 285 K in cubic spinel LiMn_2O_4 .^{14,15}

One of the popular mixed or doped ferrites is Mn ferrites. Although it is described that Mn ferrites adopt inverse spinels as Fe, Co, and Ni ferrites, experimental data indicate that it exists more likely as normal spinel with 19% of Mn^{2+} occupying octahedral sites and 81% of Mn^{2+} occupying tetrahedral sites.¹⁶ In this study, we synthesized mixed ferrite NPs between Fe and Mn and examined their magnetic behaviors. Seeds of Mn oxide NPs are used for the preparation of crystalline Fe_3O_4 and MnFe_2O_4 NPs. Verwey transition was identified in 14.5 nm Fe_3O_4 NPs. In addition, $\text{MnFe}_2\text{O}_4@\text{Mn}_x\text{Fe}_{1-x}\text{O}$ core-shell NPs were synthesized in a seed-mediated method from MnFe_2O_4 NPs. Moiré fringes were observed in the epitaxial plane-matching growth. Due to the antiferromagnetic (AFM) $\text{Mn}_x\text{Fe}_{1-x}\text{O}$ shell, there is an exchange bias with a shift of hysteresis along the field direction both in field-cooled (FC) and zero-field-cooled (ZFC) measurements. $\text{Mn}_x\text{Fe}_{1-x}\text{O}$ adopts a rock salt structure ($Fm-3m$) as MnO, FeO, and other similar divalent metal oxides. Recently, there are increasing efforts and interests in the study of $\text{Mn}_x\text{Fe}_{1-x}\text{O}$ NPs with various shapes.^{17,18} This attraction is ascribed to their resistance to oxidation compared to MnO and FeO, which

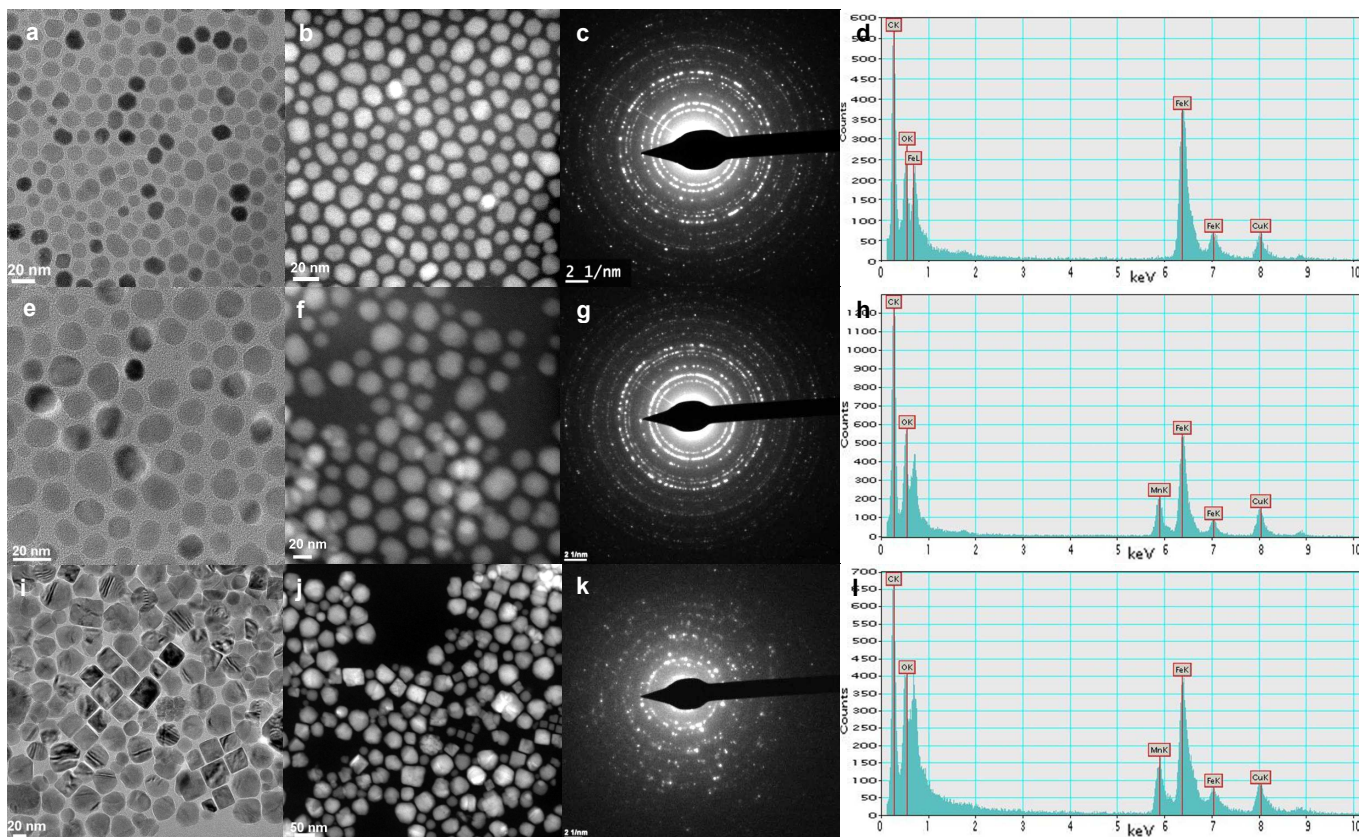


Fig. 1 (a) TEM image, (b) STEM image, (c) SAED pattern, and (d) EDX spectrum of Fe₃O₄ NPs synthesized from Mn oxide seeds. (e) TEM image, (f) STEM image, (g) SAED pattern, and (h) EDX spectrum of MnFe₂O₄ NPs synthesized from Mn oxide seeds. (i) TEM image, (j) STEM image, (k) SAED pattern, and (l) EDX spectrum of MnFe₂O₄@Mn_xFe_{1-x}O core-shell NPs synthesized from MnFe₂O₄ NPs.

extend their utilities as stable magnetic probes. Divalent metal oxides are known oxygen-rich and prone to be cation-vacancy. Diverse magnetism, and diverse electrical properties can be achieved by occupying those vacant sites with other dopants, for example as seen in electrical band gap engineering of metal oxides. Not only the unusual shell formation of Mn_xFe_{1-x}O on MnFe₂O₄ cores, we observed rich magnetism from Verwey transition, spin glass-like state, and to the exchange bias under ZFC condition during the synthesis of these metal oxide NPs.

Results and discussion

The method of generating NPs in this study is based on a colloidal wet chemistry, which is represented by nucleation and growth mechanism for the NP growth. There are physical methods such as electric explosion of wires,¹⁹ or laser target evaporation,²⁰ which utilize instruments rather than being based on the thermal decomposition solution method. Although useful for massive scale production, some of these physical methods suffer from the wide size distribution of particles compared to the bottom-up chemical methods. The controlled synthesis is required for the fundamental study of their physical meanings, especially the size effect of magnetic NPs.

Mn oxide NPs (3.6 ± 0.6 nm, Electronic Supplementary Information, Fig. S1) were used as seeds for the synthesis of Fe₃O₄ and MnFe₂O₄ NPs. XRD pattern of these seeds does not

exhibit any prominent crystalline phases (Fig. S2, ESI). With these seeds, single crystalline Fe₃O₄ NPs with a volume-

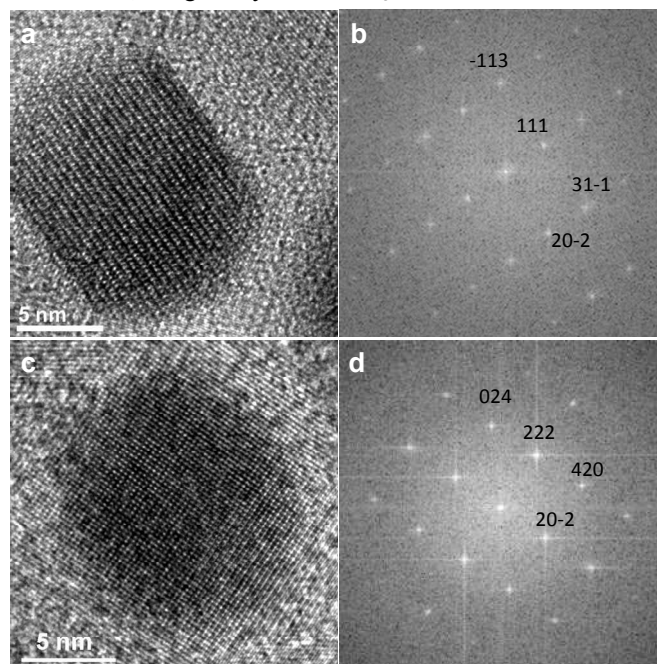


Fig. 2 (a), (c) HRTEM images of Fe₃O₄ NPs, and (b), (d) Fourier-transformed images of (a) and (c) respectively. Two HRTEM images contain the same zone axis of [-12-1].

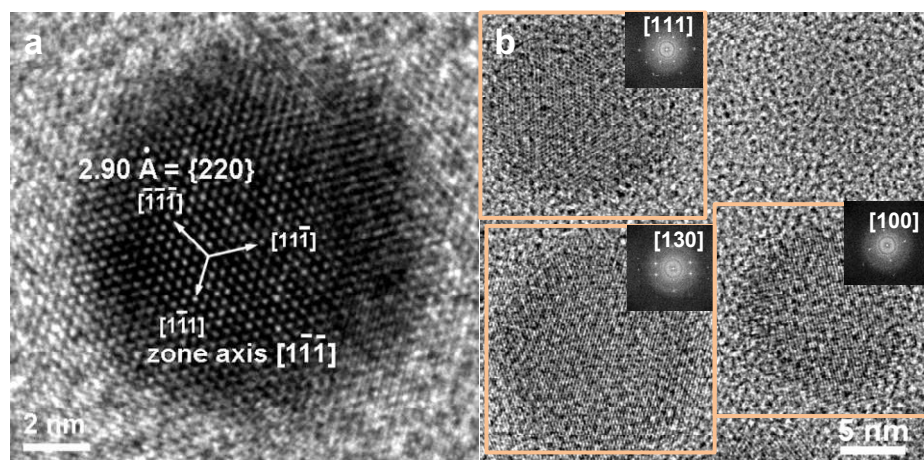


Fig. 3 HRTEM images of MnFe_2O_4 NPs. (a) Lattice planes of $\{220\}$ were identified in a single crystalline NP. (b) Three different single crystal NPs were found with the zone axes of $[111]$, $[130]$, and $[100]$ respectively.

averaged mean diameter of $14.5 (\pm 1.8)$ nm were prepared by high temperature decomposition method (Fig. 1a and 1b).²¹ Selected area electron diffraction (SAED) pattern indicates cubic spinel structure of Fe_3O_4 (Fig. 1c). These Fe_3O_4 NPs maintain single crystalline structures (Fig. 2). For example, two NPs contain the same zone axis of $[-12-1]$ but with different lattice planes of (111) ($d = 4.833$ Å) and $(20-2)$ ($d = 2.960$ Å) (Fig. 2a), and (222) ($d = 2.416$ Å) and $(20-2)$ ($d = 2.960$ Å) (Fig. 2c). Fourier-transformed images of these two NPs (Fig. 2b and 2d) prove the same zone axis of these two particles.

Similar to the synthesis of Fe_3O_4 , MnFe_2O_4 NPs were synthesized in a seed-mediated method from Mn oxide NPs. Average size of NPs is $13.2 (\pm 2.7)$ nm (Fig. 1e). In the high resolution transmission electron microscopy (HRTEM) image of MnFe_2O_4 NP in Fig. 3a, $\{220\}$ planes were observed with the zone axis of $\langle 111 \rangle$. In the face-centered cubic (fcc) structure, (110) planes are difficult to find due to the systematic absence rule. In cubic spinel structure, though, (220) planes are observable. In another TEM image in Fig. 3b, single crystalline NPs were found with three different zone axes of $[111]$, $[130]$ and $[100]$.

With MnFe_2O_4 NPs as seeds, further growth was performed using $\text{Fe}(\text{acac})_3$ (acac: acetylacetonate) and $\text{Mn}(\text{acac})_2$ as the organometallic sources. Cubic shapes were found, and Moiré fringes were observed extensively on these cubic shape NPs. Moiré fringes occur in hetero core-shell structures which are prepared by the plane-matching epitaxial growth.^{22,23} Since the deviation from equilibrium is greater in nanosize, it is easier to prepare epitaxially grown core-shell nanostructures at lower temperature. In epitaxially grown bulk films, high temperature deposition method is mostly used, while in nanosize the epitaxy growth can be achieved at room temperature. The most prominent examples are noble metal NPs, such as Pd/Pt²⁴ and Au/Pd.^{22,25}

In $\text{MnFe}_2\text{O}_4@ \text{Mn}_x\text{Fe}_{1-x}\text{O}$ NPs, lattice mismatch between the lattice parameter of $\text{Mn}_x\text{Fe}_{1-x}\text{O}$ ($Fd-3m$, $a = 4.372$ Å) and half of the lattice parameter of MnFe_2O_4 ($Fm-3m$, $a = 8.412$ Å) is 3.8%. When there is no misorientation between the lattice

planes of core and shell, spacing of Moiré fringe is related with these cell parameters and d -spacings as $D = d_1 d_2 / (d_1 - d_2)$, where D is the distance of Moiré fringes, and d_1 and d_2 are d -spacings of the specific lattice planes of core and shell materials.²² In our example, two types of Moiré fringes are observed (Fig. 4). Distances of Moiré fringes (D) in Fig. 4a and 4b are 4.0 nm, and these are close to the calculated value of 3.96 nm which is derived from (220) plane of $\text{Mn}_x\text{Fe}_{1-x}\text{O}$ ($d_1 = 1.545$ Å) and (440) plane of MnFe_2O_4 ($d_2 = 1.487$ Å). Distance of Moiré fringe in Fig. 4c is 2.0 nm, and this distance is close to the value of 1.98 nm which is derived from the

(440) plane of $\text{Mn}_x\text{Fe}_{1-x}\text{O}$ ($d_1 = 0.773$ Å) and (880) plane of MnFe_2O_4 ($d_2 = 0.744$ Å). Most NPs that are examined contain Moiré fringes with D values of 3.95 - 4.10 nm and are similar to the NPs shown in Fig. 4a and 4b. In addition, these fringes stem from $\{hh0\}$ planes of core and shell materials. Detailed analysis by HRTEM images indicates that they lie in the same $\{hh0\}$ planes of $\text{Mn}_x\text{Fe}_{1-x}\text{O}$ shells (Fig. 4d, 4e, and 4f). In addition, the fast Fourier-transformed (FFT) patterns imply that the particles are composed of $\{h00\}$ planes (zone axis $\langle 100 \rangle$, Fig. 4g and 4k) with the Moiré fringes residing on the diagonals of these cubes. Similar formation of Moiré fringes perpendicular to $\langle 110 \rangle$ direction in cubes was also identified in Pd@Ag,²⁶ Au@Pd,²² and MnZn ferrite core-shell nanocubes.²⁷ It is also known that cubic shapes are easier to be made as core-shell structures by epitaxial growth.²²

In some noble metal nanomaterials, intrinsic twins or the dislocations in the cores govern those in outer shells, and produce Moiré fringes with twin boundaries, such as Ag shell on Cu cores,²⁸ Ni@Au core-shell NPs,²⁹ and Au@Ni core-shell nanoplates.³⁰ During the deformation, twins in the cores accompany on the shell in the epitaxial growth. In metal oxides, twins are found in nanomaterials with severe deviation from equilibrium such as nanowires.³¹ Twins compensate for this deviation and provide shape stability to 1D nanostructures, as was demonstrated in the recent theoretical study.³² In spherical metal oxide NPs, twins are hardly observed, and the Moiré fringes in $\text{MnFe}_2\text{O}_4@ \text{Mn}_x\text{Fe}_{1-x}\text{O}$ NPs derive from the difference of lattice spacings between core and shell during the epitaxial growth. Reconstructed images after filtering the (110) planes in the respective FFT patterns reveal the highlighted fringes (Fig. 4h, 4j, and 4l). The slight distorted fringes stem from the deformation of core-shell structure during the epitaxial growth. The origin of this deformation can be the load exerted by the shell on the cores, or can be the strain in the shell which is induced during the core-shell formation. In particular, the strain existing in the shell due to the lattice mismatch between core and shell (3.8 %) is thought to play the major roles in the formation of distorted Moiré fringes.

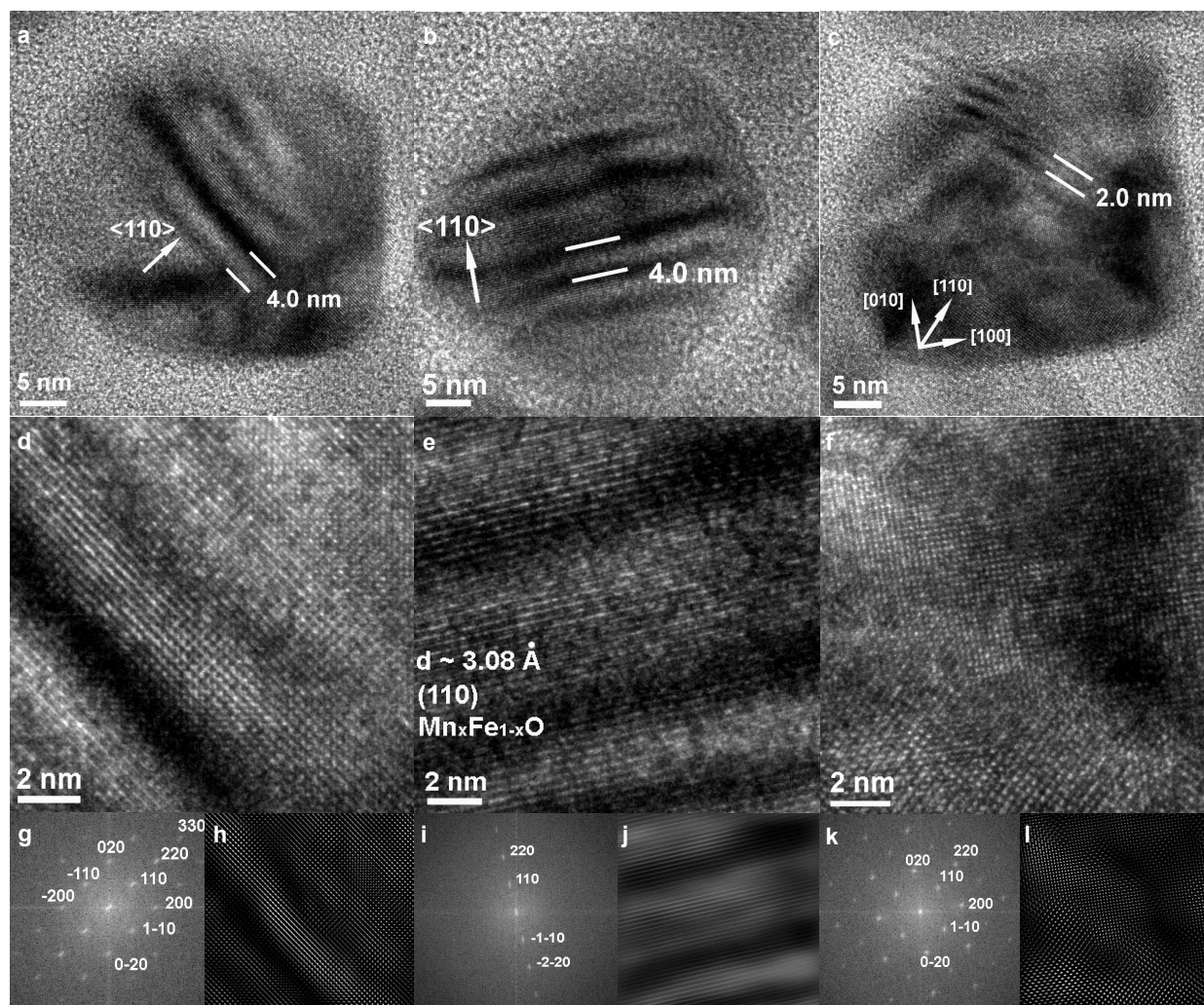


Fig. 4 TEM images of $\text{MnFe}_2\text{O}_4@ \text{Mn}_x\text{Fe}_{1-x}\text{O}$ core-shell NPs (a), (b) with a Moiré fringe distance of 4.0 nm and (c) with a Moiré fringe distance of 2.0 nm. (d), (e), (f) HRTEM images corresponding to TEM images of (a), (b), (c), respectively. (g) Fourier-transformed diffraction pattern and (h) reconstructed image after filtering FFT pattern of (d). (i) Fourier-transformed diffraction pattern and (j) reconstructed image after filtering FFT pattern of (e). (k) Fourier-transformed diffraction pattern and (l) reconstructed image after filtering FFT pattern of (f).

In XRD patterns, Fe_3O_4 is refined as cubic spinel with a space group of $Fd-3m$ and with a cell parameter of $a = 8.372 \text{ \AA}$ (top, Fig. 5a), which is slightly larger than in normally observed Fe_3O_4 NPs ($\sim 8.356 \text{ \AA}$),^{33,34} but smaller than in bulk magnetite (8.394 \AA , JCPDS # 79-0417). The structure of MnFe_2O_4 was also determined by Rietveld refinement with a cell parameter of $a = 8.426 \text{ \AA}$ (middle, Fig. 5a). In addition, the phase exists as Fe-rich $\text{Mn}_{0.76}\text{Fe}_{2.24}\text{O}_4$ based on the refinement, which is agreeable with a recent study about the variation of cell parameters of spinel ferrites depending on the compositional ratio between Mn and Fe.³⁴ XRD pattern of $\text{MnFe}_2\text{O}_4@ \text{Mn}_x\text{Fe}_{1-x}\text{O}$ core-shell NPs comprises two phases of spinel ferrite ($Fd-3m$) and rock salt ($Fm-3m$) structures (bottom, Fig. 5a). Peak deconvolution with pseudo-Voigt curve fitting indicates that the cell parameter of MnFe_2O_4 in $\text{MnFe}_2\text{O}_4@ \text{Mn}_x\text{Fe}_{1-x}\text{O}$ core-shell NPs is 8.412 \AA , and that of $\text{Mn}_x\text{Fe}_{1-x}\text{O}$ is 4.372 \AA (Fig. 5b). After Rietveld refinement, slight Fe-rich $\text{Mn}_{0.465}\text{Fe}_{0.527}\text{O}$ with cation vacancy was identified. Both MnO and FeO are known as a rock salt structure with a cell parameter of $a = 4.447 \text{ \AA}$ for

MnO ,³⁵ and $a = 4.326 \text{ \AA}$ for FeO .³⁶ Bulk MnO has a Neel temperature (T_N) of 118 K .^{35,37} FeO shows rather high T_N of 195 K .³⁸ It exists non-stoichiometric with hardly being FeO due to its vulnerable nature to the oxidation. Stoichiometry also plays roles in the appearance of T_N , as lower T_N is observed in more off-stoichiometric FeO.³⁸

Scherrer equation ($t = 0.9\lambda / \beta \cos\theta$, where t is the domain thickness, λ is the wavelength of X-ray source ($\text{CuK}\alpha$, 1.54056 \AA), β is the full width at the half maximum intensity as radian, and θ is the Bragg angle) is a useful method for identifying domain size of the analysed materials. From the XRD pattern of Fe_3O_4 ($a = 8.372 \text{ \AA}$), domain thickness of $t = 15.2 \text{ nm}$ was calculated at (311) plane ($2\theta = 35.534$). This is an important indication of the overall size of NPs examined in this study, and the value (15.2 nm) is slightly larger than the size obtained in the TEM image ($14.5 \pm 1.8 \text{ nm}$). As the size of ferrite decreases, the Verwey temperature is known to decrease and the transition is smooth.³⁹ For example, Verwey transition was

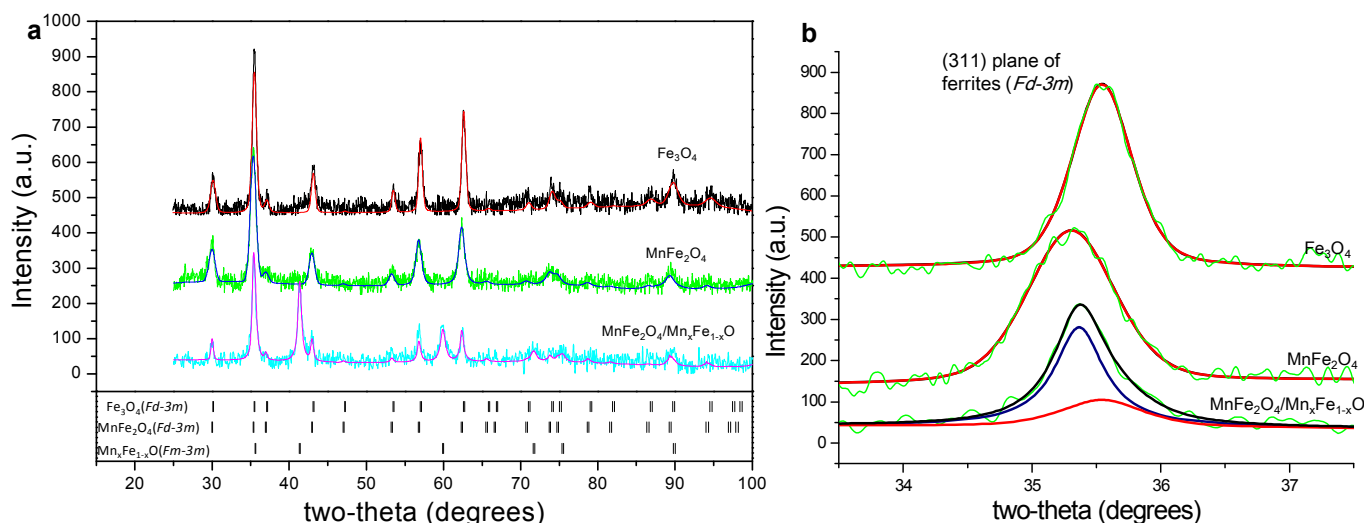


Fig. 5 (a) XRD patterns with Rietveld refinements of (top) Fe_3O_4 , (middle) MnFe_2O_4 , and (bottom) $\text{MnFe}_2\text{O}_4@Mn_x\text{Fe}_{1-x}\text{O}$ core-shell NPs. (b) Peak deconvolution with pseudo-Voigt curve fitting of (311) planes of ferrites ($Fd-3m$) and (111) plane of $Mn_x\text{Fe}_{1-x}\text{O}$ ($Fm-3m$).

observed as first-order transition around at 90 K in 9 nm ferrite NPs.⁴⁰

Magnetism of NPs follows the pattern of soft ferromagnetism (FM) with a large spontaneous magnetization. Although there is a dipolar interaction, the saturation magnetization of 14.5 nm Fe_3O_4 NPs reaches 168 emu/g at 5 K, and 152 emu/g at 300 K in field-dependent (M - H) measurement (Fig. 6b). In 13.2 nm MnFe_2O_4 NPs, saturation magnetization reaches 136 emu/g at 5 K (Fig. 6d). Slight decrease of magnetization was observed in $\text{MnFe}_2\text{O}_4@Mn_x\text{Fe}_{1-x}\text{O}$ core-shell NPs with 118 emu/g at 5 K, and 96 emu/g at 300 K (Fig. 6f).

There are some anomalies in temperature-dependent magnetization (M - T). In Fe_3O_4 NPs, Verwey transition with a sharp drop of magnetization was observed at around 96 K (Fig. 6a). This sharp drop is related with the high crystallinity of particles, or with the presence of interparticle interaction. With the decrease of particle size, charge ordering is known not as efficient and not as fast as in the bulk magnetite, which makes a smooth decrease of magnetic susceptibility around the transition.^{39,40} Also noteworthy in M - T curve of Fe_3O_4 NPs is the small broad mound centered at 35 K in ZFC measurement. In Fe_3O_4 NPs with a sharp decrease of magnetization such as in our study, this broad mound is regularly observed.⁴⁰ One reason would be the glass-like transition with a sharp decrease of magnetization, which is caused by electrical low temperature tunnelling.⁴¹ The other assumption is that there is a partial surface oxidation in Fe_3O_4 . Single crystalline plate shape $\gamma\text{-Fe}_2\text{O}_3$ NPs with sizes of 9-10 nm contain spin-disordered surface with 0.6 nm thickness.⁴² Fe_3O_4 is more vulnerable to the oxidation, and it is thought that disordered surface spins in partially oxidized shell interact with magnetically ordered FM core spins during the freezing process and cause the decrease of susceptibility with a broad transition at 35 K.

In M - T curve of MnFe_2O_4 NPs, the magnetic behaviour follows spin glass-like state (Fig. 6c). Below around 110 K,

sharp decrease of magnetization in ZFC measurement is observed from 34.3 emu/g at 116 K to 4.3 emu/g at 5 K. This decrease of susceptibility is due to the dominant disordered spins during the freezing process. Spin glass is well observed in two phase systems, popularly in AFM-FM hybrid materials.⁴³ Inhomogeneous phases in Fe-rich $Mn_x\text{Fe}_{3-x}\text{O}_4$ NPs are presumed to cause such spin glass transitions. Broad blocking temperature (T_B) is also found with no irreversibility at 300 K between ZFC and FC measurements (inset, Fig. 6c). Broad T_B in more general terms is associated with the large size distribution of NPs, owing to its well-known correlation with the volume of particles. In our example, this broad transition is presumed due to the competition between two different magnetizations. There is a sudden decrease of susceptibility below 110 K, and this decrease is caused by the collapse of this competition and by the random spin orientation under ZFC measurement. In ZFC condition, there are zero applied fields and it is not able to hold spin orientation during the cooling process. Frustration of spins is also illustrated in FC measurement, in which broad mound appears with the slight increase of susceptibility. In FC condition, spins are locked oriented by cooling, and the susceptibility tends to increase at lower temperature because thermal energy is not enough to disturb spin orientation. Slight increase of magnetization in FC means that there is an intraparticle interaction, which becomes larger with the increase of temperature. The magnetization that contributes to this intraparticle interaction is not necessarily AFM-FM, as materials with strong soft FM exhibit the spin glass-like properties.⁴⁴ M - T curve of FC measurement generates power law fit with $M(T) = M_0(1 - T/T_c)^\beta$, which indicates the Curie temperature (T_c) of 363 K (inset, Fig. 6c). There is also no irreversibility between ZFC and FC measurements, and this is in the more general terms thought due to the existence of short range ordering.⁴⁵ This ordering contributes differently to the total magnetization under ZFC and FC, thus provides non-overlapping curves. The intraparticle interaction is also

witnessed in the slight asymmetric loop shift of M - H curve under ZFC condition at 5 K (471 Oe, -563 Oe, inset, Fig. 6d). Mn oxide seed NPs and Fe-rich MnFe_2O_4 phase are believed to cause these irregular magnetic behaviours.

In a study of magnetite NPs which were synthesized by biomineralization, Verwey transition was observed at 105 K and the chain-like arrangement of NPs makes the transition sharp.⁹ Chainlike proximity and collective particle correlation cause spontaneous charge ordering between Fe^{2+} and Fe^{3+} , and during this fast charge ordering, sharp decrease of magnetization occurs. Another study reported that the applied field (0.25 tesla) during the synthesis causes partial oxidation of Fe^{2+} ions and removes the chance of electron hopping and charge ordering of Fe^{2+} and Fe^{3+} , so that no transition was observed.⁸ There is a controversy whether spontaneous charge ordering of Fe^{2+} and Fe^{3+} causes lattice distortion and unit cell change, or unit cell change from cubic to lower symmetry causes charge ordering.⁴⁶ In fact, unlike the unit cell change which can be identified with various x-ray techniques, charge ordering is controversial for its existence due to the experimental limitations.⁴⁷

In M - T curve of $\text{MnFe}_2\text{O}_4@Mn_xFe_{1-x}O$ core-shell NPs, there are two transitions at 163 K and 45 K (Fig. 6e). The

magnetic moment is 18.2 emu/g in ZFC, and 30.3 emu/g in FC measurements at 5 K ($H_c = 100$ Oe), and these moments are large considering AFM $\text{Mn}_x\text{Fe}_{1-x}\text{O}$ shell. This is not simply due to the presence of FM MnFe_2O_4 , and more likely due to FM-AFM interaction between MnFe_2O_4 and $\text{Mn}_x\text{Fe}_{1-x}\text{O}$. As seen in the exchange bias in Fig. 7, AFM-FM interaction causes large number of interface spins of AFM $\text{Mn}_x\text{Fe}_{1-x}\text{O}$ shell to align ferromagnetically with core spins of MnFe_2O_4 . At the transition around 163 K, there is a sharp increase of magnetization in ZFC measurement. This is typical of AFM-PM transition, as linear pattern conforming to the Curie-Weiss law is observed over 163 K in the curve of $1/M$ vs T with FC data (inset, Fig. 6e). This sharp transition at 163 K is reminiscent of AFM FeO, as seen in several examples of FeO ,⁴⁸⁻⁵⁰ $\text{Mn}_x\text{Fe}_{1-x}\text{O}$,¹⁸ and $\text{FeO}/\text{Fe}_3\text{O}_4$ core-shell NPs.⁵¹ The content of Mn affects the decrease of transition temperature compared to T_N (195 K) of FeO, for example 173 K in $\text{Mn}_{0.29}\text{Fe}_{0.71}\text{O}$ NPs,⁵¹ and 157 K in $\text{Mn}_{0.50}\text{Fe}_{0.50}\text{O}$ NPs.⁵² However, soft FM at 300 K in M - H curve (Fig. 6f) and high magnetization (26.5 emu/g, $H_c = 100$ Oe) in M - T curve at 300 K (Fig. 6e) imply that $\text{MnFe}_2\text{O}_4@Mn_xFe_{1-x}O$ core-shell NPs do not simply exist as PM at 300 K. The irreversibility between ZFC and FC is another factor to consider as FM at 300 K. This magnetization is believed a sum

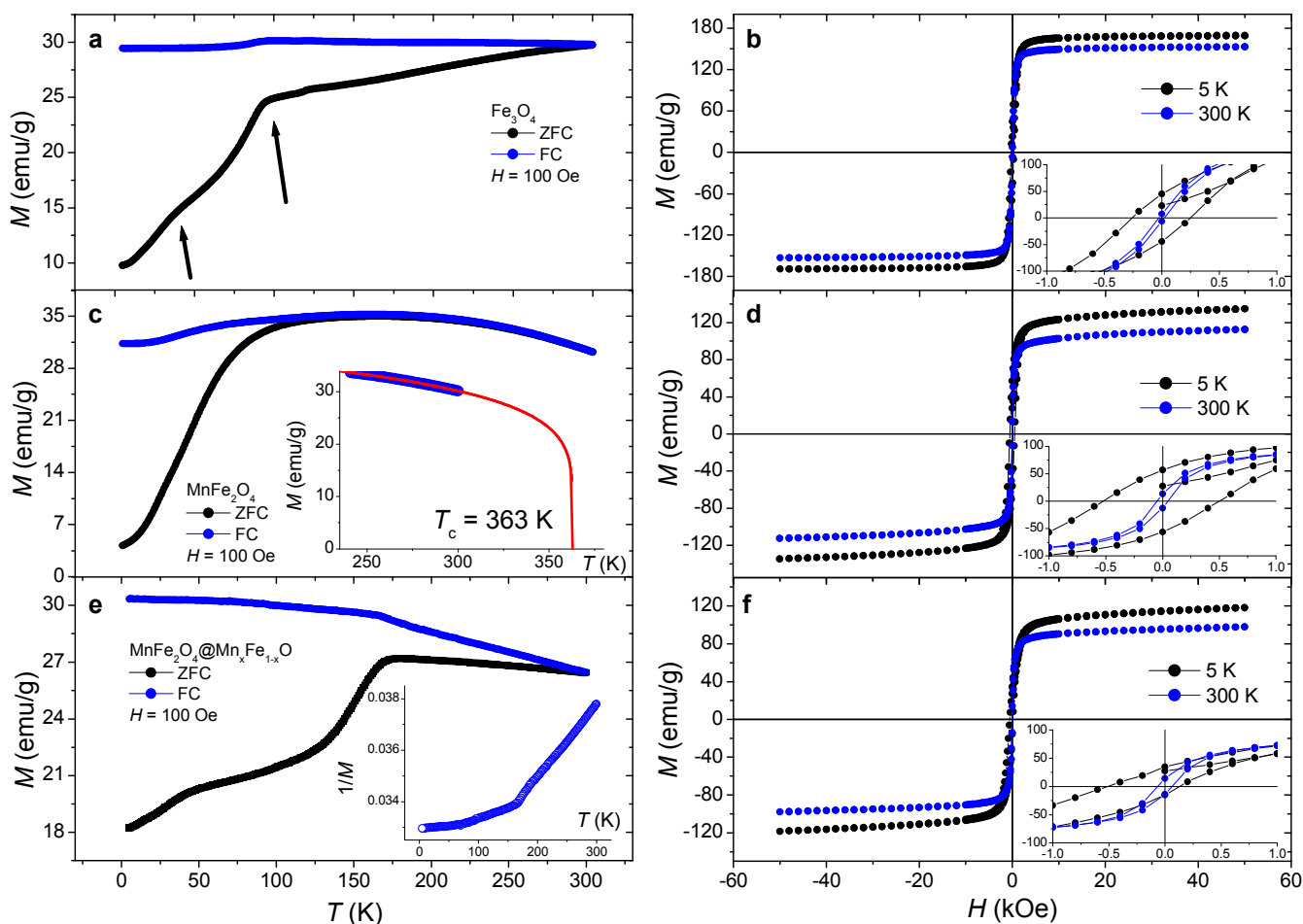


Fig. 6 (a) Temperature and (b) field-dependent magnetic measurements of Fe_3O_4 NPs. (c) Temperature and (d) field-dependent magnetic measurements of MnFe_2O_4 NPs. (e) Temperature and (d) field-dependent magnetic measurements of $\text{MnFe}_2\text{O}_4@Mn_xFe_{1-x}O$ core-shell NPs.

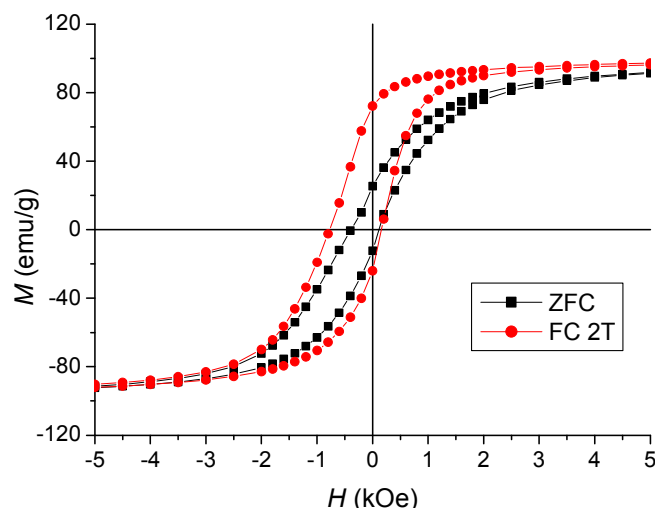


Fig. 7 Field-dependent magnetization of $\text{MnFe}_2\text{O}_4@Mn_x\text{Fe}_{1-x}\text{O}$ core-shell NPs. The measurement was conducted at 5 K with zero-field-cooled (ZFC) first, followed by field-cooled (FC) measurement.

of two phases of FM MnFe_2O_4 cores and AFM $\text{Mn}_x\text{Fe}_{1-x}\text{O}$ shells. The other transition at 45 K is due to AFM-FM interaction, as was observed in $\text{Mn}_x\text{Fe}_{1-x}\text{O}$ nanoplates with significant MnFe_2O_4 .⁵² This transition is more obvious under ZFC condition, in which sample was cooled with zero applied fields. Small applied field (100 Oe) is enough to align those spins around AFM-FM interfaces due to the soft magnetic nature of cores. Another characteristic of this transition at 45 K is its broadness ranging from 25 K to 80 K. This broad transition is believed from many different AFM-FM interactions in $\text{MnFe}_2\text{O}_4@Mn_x\text{Fe}_{1-x}\text{O}$ core-shell NPs. Different interactions are caused by the broad size distribution or by the variable stoichiometry of $\text{Mn}_x\text{Fe}_{1-x}\text{O}$ shell, as more off-stoichiometry produces broader magnetic transitions.⁵³ Large average size (39.2 ± 9.3 nm) with broad size distribution reflects the inhomogeneity of $\text{MnFe}_2\text{O}_4@Mn_x\text{Fe}_{1-x}\text{O}$ core-shell NPs.

To further investigate the nature of FM-AFM interaction of $\text{MnFe}_2\text{O}_4@Mn_x\text{Fe}_{1-x}\text{O}$ core-shell NPs, M - H measurements at 5 K were performed (Fig. 7). In ZFC measurement, sample was cooled from 300 K to 5 K under zero fields, followed by the measurement in between ± 20 kOe. In FC measurement, sample was cooled from 300 K to 5 K under the applied magnetic field of 20 kOe, followed by M - H measurement. In both FC and ZFC measurements, hysteresis shifts and asymmetric lobes were observed, but with a larger shift and enhanced coercivity under FC condition (Fig. 7). Hysteresis shift in ZFC condition in Fig. 7 means that the FM/AFM interaction in demagnetized state or under zero-field state is strong enough to exhibit anisotropy.⁵⁴ Metallic cobalt core and its oxidized shell is a prominent example for enhancing anisotropy by exchange bias.⁵⁵ It has been reported that some doped ferrites show extraordinary magnetization especially when small amount of Mn^{2+} , Zn^{2+} , and Cu^{2+} are added. Since octahedral sites are occupied by even number of Fe^{2+} and Fe^{3+} in inverse spinel, those doped ions

which were replaced with Fe^{2+} undergo FM interaction with other octahedral Fe^{3+} . This enhanced magnetic interaction leads to the increase of spontaneous magnetization in doped ferrites.

Experimental

All chemicals and solvents were analytical grades and used without further purification from commercial sources (Sigma-Aldrich). Powder XRD measurements were performed with a Philips Panalytical X'Pert Pro X-ray powder diffractometer (40 V, 40 mA, $\text{CuK}\alpha$ $\lambda = 1.54056$ Å) in a θ - θ mode from 25 to 100 degrees (2θ). TEM images were obtained with either Tecnai G2 Spirit TWIN, 20-120 kV/LaB6 Transmission Electron Microscope, or FEI Titan 80-300 kV S/TEM using field emission gun operating at 300 kV. Scanning transmission electron microscopy (STEM) imaging was carried out with FEI Titan 80-300 kV S/TEM. The measurement was performed with high-angle annular dark field (HAADF) detector by adjusting the camera length to 190 mm and spot size to 6. Sample was dispersed in 0.1 mL of hexane and was sonicated for 30 seconds before dropcasting onto carbon-coated Cu grids. Magnetic properties were measured with Superconducting Quantum Interference Device (SQUID, Quantum Design, Inc. San Diego, CA, USA). For the measurement of magnetic susceptibility, sample was dried under vacuum for 1 h before the measurement. Without using diamagnetic matrix for dispersing particles, the dried sample with sufficiently large mass (3.5 mg in case of Fe_3O_4 NPs) was measured.

Synthesis of Mn oxide NPs

$\text{MnCl}_2 \cdot 4\text{H}_2\text{O}$ (1.0 g, 5.05 mmol), oleylamine (3.6 mL, 10.9 mmol), and oleic acid (3.6 mL, 11.4 mmol) were mixed with octyl ether (8.0 mL). Under air condition, reaction mixture was stirred at room temperature for 10 minutes before temperature was increased to 200 °C. Stirring continued for 0.5 hours at 200 °C. Then, temperature was further increased to 280 °C, and stirring continued for additional 1 hour. After the reaction mixture was cooled down, hexane (5.0 mL) was added to disperse the products. Particles were not precipitated with excess EtOH, and these particles in hexane dispersion were used as seeds without further purification.

Synthesis of 14.5 nm Fe_3O_4 NPs

Mixture of hexane-dispersed Mn oxide NPs (180 μL), $\text{Fe}(\text{acac})_3$ (850 mg, 2.41 mmol), oleylamine (1.8 mL, 5.5 mmol), oleic acid (1.8 mL, 5.7 mmol), 1,2-hexadecanediol (2.4 g, 9.28 mmol) was stirred in the presence of octyl ether (8.0 mL). Under N_2 atmosphere, reaction temperature was increased to 200 °C and the mixture was stirred for 0.5 hours. Temperature was increased to 285 °C and the mixture was stirred for 2 hours. Then, reaction temperature was further increased to 325 °C and stirring continued for 0.5 hours. After the reaction mixture was cooled down, the precipitates were collected by adding 8 mL of hexane and 20 mL of EtOH, followed by centrifugation at 4000 rpm for 5 minutes. Washing and precipitation steps were repeated (x 2) to obtain Fe_3O_4 NPs.

Synthesis of 13.2 nm MnFe₂O₄ NPs

Other conditions are the same as the synthesis of Fe₃O₄ NPs except the molar ratio of reaction mixture, which was prepared by mixing hexane-dispersed Mn oxide NPs (150 μL), Fe(acac)₃ (450 mg, 1.27 mmol), Mn(acac)₂ (150 mg, 0.59 mmol) oleylamine (1.0 mL, 3.04 mmol), oleic acid (1.0 mL, 3.17 mmol), and 1,2-hexadecanediol (1.8 g, 6.96 mmol).

Synthesis of 39.2 nm MnFe₂O₄@Mn_xFe_{1-x}O core-shell NPs

Mixture of hexane-dispersed MnFe₂O₄ NPs (250 μL), Fe(acac)₃ (450 mg, 1.27 mmol), Mn(acac)₂ (320 mg, 1.27 mmol) oleylamine (1.8 mL, 5.5 mmol), oleic acid (1.8 mL, 5.7 mmol), and 1,2-hexadecanediol (2.4 g, 9.28 mmol) was stirred with octyl ether (8.0 mL). Under N₂ atmosphere, reaction temperature was increased to 200 °C and the mixture was stirred for 2 hours. Temperature was further increased to 280 °C and stirring continued for 2.5 hours. Finally, temperature was increased to 325 °C and stirring continued for 0.5 hours. After the reaction mixture was cooled down, the precipitates were collected by adding 8 mL of hexane and 20 mL of ethanol, followed by centrifugation at 4000 rpm for 5 minutes. Washing and precipitation steps were repeated (x 2) to obtain MnFe₂O₄@Mn_xFe_{1-x}O core-shell NPs.

Conclusions

New approach to the synthesis of Fe₃O₄ and MnFe₂O₄ NPs was devised starting from Mn oxide seeds. Though they exhibit singular structural characteristics on HRTEM, some unexpected magnetic behaviours are observed. Fe₃O₄ NPs with a diameter of 14.5 nm display Verwey transition at 96 K with a sharp drop of magnetization, and MnFe₂O₄ NPs display spin glass-like state at low temperature. Epitaxially grown MnFe₂O₄@Mn_xFe_{1-x}O core-shell NPs were synthesized from MnFe₂O₄ NPs, and there are Moiré fringes especially on the cubic shape NPs. This approach will be another demonstration of synthetic method for magnetically active, and magnetically diverse soft ferrite nanomaterials.

Acknowledgements

Financial support is gratefully acknowledged from Dong-A University, King Abdullah University of Science and Technology (KAUST), and NSF Grant DBI-1266377. The work at UCLA also leveraged the support provided by the National Science Foundation and the Environmental Protection Agency under Cooperative Agreement Number, DBI 0830117.

Notes and references

^a Department of Chemistry, Dong-A University, Busan 604-714, South Korea. E-mail: hyonmin1@dau.ac.kr

^b Department of Chemistry and Biochemistry, University of California, Los Angeles, California 90095-1569, United States.

^c Division of Physical Sciences and Engineering, and Center for Advance Membranes and Porous Materials (AMPM), 4700 King Abdullah University of Science and Technology, Thuwal 23955-6900, Kingdom of Saudi Arabia.

Electronic Supplementary Information (ESI) available: XRD, TEM, STEM, and size distribution of synthesized nanoparticles. See DOI: 10.1039/b000000x/

1. F. Gazeau, J. C. Bacri, F. Gendron, R. Perzynski, Y. L. Raikher, V. I. Stepanov and E. Dubois, *J. Magn. Magn. Mater.*, 1998, **186**, 175-187.
2. H. Rudolf, D. Silvio, M. Robert and Z. Matthias, *J. Phys.: Condens. Matter*, 2006, **18**, S2919.
3. F. Kools and P. J. van der Valk, in *Kirk-Othmer Encyclopedia of Chemical Technology*, John Wiley & Sons, Inc., 2000, pp. 55-91.
4. A. Broese van Groenou, P. F. Bongers and A. L. Stuyts, *Mater. Sci. Eng.*, 1969, **3**, 317-392.
5. E. J. Verwey, P. W. Haayman and F. C. Romeijn, *J. Chem. Phys.*, 1947, **15**, 181-187.
6. E. J. W. Verwey, *Nature*, 1939, **144**, 327-328.
7. G. F. Goya, T. S. Berquo, F. C. Fonseca and M. P. Morales, *J. Appl. Phys.*, 2003, **94**, 3520-3528.
8. J. Wang, Q. Chen, X. Li, L. Shi, Z. Peng and C. Zeng, *Chem. Phys. Lett.*, 2004, **390**, 55-58.
9. R. Prozorov, T. Prozorov, S. K. Mallapragada, B. Narasimhan, T. J. Williams and D. A. Bazylinski, *Phys. Rev. B*, 2007, **76**, 054406.
10. V. A. M. Brabers, F. Walz and H. Kronmüller, *Phys. Rev. B*, 1998, **58**, 14163-14166.
11. J. J. Bartel and J. E. F. Westrum, *AIP Conf. Proc.*, 1973, **10**, 1393-1397.
12. J. J. Bartel and J. E. F. Westrum, *AIP Conf. Proc.*, 1975, **24**, 86-87.
13. J. B. Yang, X. D. Zhou, W. B. Yelon, W. J. James, Q. Cai, K. V. Gopalakrishnan, S. K. Malik, X. C. Sun and D. E. Nikles, *J. Appl. Phys.*, 2004, **95**, 7540-7542.
14. Y. Shimakawa, T. Numata and J. Tabuchi, *J. Solid State Chem.*, 1997, **131**, 138-143.
15. A. S. Wills, N. P. Raju and J. E. Greedan, *Chem. Mater.*, 1999, **11**, 1510-1518.
16. F. W. Harrison, W. P. Osmond and R. W. Teale, *Phys. Rev.*, 1957, **106**, 865-866.
17. P.-Y. Lee, H.-S. Teng and C.-S. Yeh, *Nanoscale*, 2013, **5**, 7558-7563.
18. Z. Li, Y. Ma and L. Qi, *CrystEngComm*, 2014, **16**, 600-608.
19. G. V. Kurlyandskaya, I. Madinabeitia, I. V. Beketov, A. I. Medvedev, A. Larranaga, A. P. Safronov and S. M. Bhagat, *J. Alloy. Compd.*, 2014, **615**, S231-S235.
20. A. P. Safronov, I. V. Beketov, S. V. Komogortsev, G. V. Kurlyandskaya, A. I. Medvedev, D. V. Leiman, A. Larrañaga and S. M. Bhagat, *AIP Adv.*, 2013, **3**, 052135.
21. S. Sun and H. Zeng, *J. Am. Chem. Soc.*, 2002, **124**, 8204-8205.
22. F.-R. Fan, D.-Y. Liu, Y.-F. Wu, S. Duan, Z.-X. Xie, Z.-Y. Jiang and Z.-Q. Tian, *J. Am. Chem. Soc.*, 2008, **130**, 6949-6951.
23. Y. Ding, X. Y. Kong and Z. L. Wang, *J. Appl. Phys.*, 2004, **95**, 306-310.
24. M. Grzelczak, J. Pérez-Juste, F. J. G. de Abajo and L. M. Liz-Marzán, *J. Phys. Chem. C*, 2007, **111**, 6183-6188.
25. Y. Yu, Q. Zhang, B. Liu and J. Y. Lee, *J. Am. Chem. Soc.*, 2010, **132**, 18258-18265.
26. C. Zhu, J. Zeng, J. Tao, M. C. Johnson, I. Schmidt-Krey, L. Blubaugh, Y. Zhu, Z. Gu and Y. Xia, *J. Am. Chem. Soc.*, 2012, **134**, 15822-15831.

27. L. Wang, X. Wang, J. Luo, B. N. Wanjala, C. Wang, N. A. Chernova, M. H. Engelhard, Y. Liu, I.-T. Bae and C.-J. Zhong, *J. Am. Chem. Soc.*, 2010, **132**, 17686–17689.
28. C. Langlois, D. Alloyeau, Y. Le Bouar, A. Loiseau, T. Oikawa, C. Mottet and C. Ricolleau, *Faraday Discuss.*, 2008, **138**, 375–391.
29. H. She, Y. Chen, X. Chen, K. Zhang, Z. Wang and D.-L. Peng, *J. Mater. Chem.*, 2012, **22**, 2757–2765.
30. L. Huang, A. Shan, Z. Li, C. Chen and R. Wang, *CrystEngComm*, 2013, **15**, 2527–2531.
31. Y. Dai, Y. Zhang, Y. Q. Bai and Z. L. Wang, *Chem. Phys. Lett.*, 2003, **375**, 96–101.
32. J. Y. Wu, S. Nagao, J. Y. He, and Z. L. Zhang, *Nano Lett.*, 2011, **11**, 5264–5273.
33. Y. V. Kolen'ko, M. Bañobre-López, C. Rodríguez-Abreu, E. Carbó-Argibay, A. Sailsman, Y. Piñeiro-Redondo, M. F. Cerqueira, D. Y. Petrovykh, K. Kovnir, O. I. Lebedev and J. Rivas, *J. Phys. Chem. C*, 2014, **118**, 8691–8701.
34. F. L. Deepak, M. Bañobre-López, E. Carbo-Argibay, M. F. G. Cerqueira, Y. Piñeiro-Redondo, J. Rivas, C. M. Thompson, S. Kamali, C. Rodríguez-Abreu, K. Kovnir and Y. V. Kolen'ko, *J. Phys. Chem. C*, 2015, **119**, 11947–11957.
35. B. Morosin, *Phys. Rev. B*, 1970, **1**, 236–243.
36. H. Fjellvåg, F. Grønvdal, S. Stølen and B. Hauback, *J. Solid State Chem.*, 1996, **124**, 52–57.
37. C. G. Shull, W. A. Strauser and E. O. Wollan, *Phys. Rev.*, 1951, **83**, 333–345.
38. F. Schrettle, C. Kant, P. Lunkenheimer, F. Mayr, J. Deisenhofer and A. Loidl, *Eur. Phys. J. B*, 2012, **85**, 164.
39. J. S. Salazar, L. Perez, O. de Abril, L. T. Phuoc, D. Ihiwakrim, M. Vazquez, J.-M. Greneche, S. Begin-Colin and G. Pourroy, *Chem. Mater.*, 2011, **23**, 1379–1386.
40. G. Muscas, G. Concas, C. Cannas, A. Musinu, A. Ardu, F. Orrù, D. Fiorani, S. Laureti, D. Rinaldi, G. Piccaluga and D. Peddis, *J. Phys. Chem. C*, 2013, **117**, 23378–23384.
41. F. Schrettle, S. Krohns, P. Lunkenheimer, V. A. M. Brabers and A. Loidl, *Phys. Rev. B*, 2011, **83**, 195109.
42. B. Martínez, X. Obradors, L. Balcells, A. Rouanet and C. Monty, *Phys. Rev. Lett.*, 1998, **80**, 181–184.
43. S. Lei, L. Liu, C. Wang, X. Shen, D. Guo, C. Wang, S. Zeng, B. Cheng, Y. Xiao and L. Zhou, *CrystEngComm*, 2014, **16**, 1322–1333.
44. B. M. Concha, R. D. Zysler and H. Romero, *Physica B: Condens. Matter*, 2006, **384**, 274–276.
45. T. Zhu, B. G. Shen, J. R. Sun, H. W. Zhao and W. S. Zhan, *Appl. Phys. Lett.*, 2001, **78**, 3863–3865.
46. D. J. Huang, H. J. Lin, J. Okamoto, K. S. Chao, H. T. Jeng, G. Y. Guo, C. H. Hsu, C. M. Huang, D. C. Ling, W. B. Wu, C. S. Yang and C. T. Chen, *Phys. Rev. Lett.*, 2006, **96**, 096401.
47. J. García, G. Subías, M. G. Proietti, J. Blasco, H. Renevier, J. L. Hodeau and Y. Joly, *Phys. Rev. B*, 2001, **63**, 054110.
48. C.-J. Chen, R.-K. Chiang, H.-Y. Lai and C.-R. Lin, *J. Phys. Chem. C*, 2010, **114**, 4258–4263.
49. A. Lak, M. Kraken, F. Ludwig, A. Kornowski, D. Eberbeck, S. Sievers, F. J. Litterst, H. Weller and M. Schilling, *Nanoscale*, 2013, **5**, 12286–12295.
50. H. Khurshid, S. Chandra, W. Li, M. H. Phan, G. C. Hadjipanayis, P. Mukherjee and H. Srikanth, *J. Appl. Phys.*, 2013, **113**, 17B508.
51. C.-C. Huang, C.-N. Chang and C.-S. Yeh, *Nanoscale*, 2011, **3**, 4254–4260.
52. H.-M. Song, J. I. Zink and N. M. Khashab, *J. Phys. Chem. C*, 2015, **119**, 10740–10748.
53. R. P. Haggerty and R. Seshadri, *J. Phys.: Condens. Matter*, 2004, **16**, 6477–6484.
54. B. Wang, Y. Liu, P. Ren, B. Xia, K. Ruan, J. Yi, J. Ding, X. Li and L. Wang, *Phys. Rev. Lett.*, 2011, **106**, 077203.
55. S. Gangopadhyay, G. C. Hadjipanayis, C. M. Sorensen and K. J. Klabunde, *J. Appl. Phys.*, 1993, **73**, 6964–6966.

TOC Figure

Rich magnetism was observed in a series of magnetic nanoparticles prepared by the seeded growth from Mn oxide nanoparticles.

